1 **Adipocyte lipolysis abrogates skin fibrosis in a Wnt/DPP4-dependent manner**
2
3 Inhibition of adipocyte lipolysis promotes fibrosis.
4
5 [1]Jussila, A.[#]; [2]Caves E.[#], [1]Zhang B., [1]Kirti, S. [1]Steele, M.; [2]Lei, V. [1]Hamburg-Shields, E.;
6 [3]Lydon, J. ,[3]Ying, Y., [4]Lafyatis, R, [5]Rajagopalan, S., [2]Horsley, V.*, [1,6,7]Atit, R.P.*
7
8 [1]Dept. of Biology, Case Western Reserve University, Cleveland, Ohio, USA
9 [2]Dept. of Molecular and Cell Biology, Yale University, New Haven, Connecticut, USA
10 [3]Dept. of Molecular and Cellular Biology, Baylor College of Medicine, Houston, Texas,
11 USA
12 [4] Department of Medicine, Division of Rheumatology and Clinical Immunology, Pittsburgh,
13 Pennsylvania, USA
14 [5] Division of Cardiovascular Medicine, University Hospitals, Harrington Heart and
15 Vascular Institute (HHVI), and Case Cardiovascular Research Institute, Department of
16 Internal Medicine and Radiology Case Western Reserve University, Cleveland, OH
17 [6]Dept. of Genetics and Genome Sciences, [7]Depts of Dermatology, Case Western
18 Reserve University, Cleveland, OH
19
20 * Corresponding Senior Authors
21 # Co-First Authors

22 **Tissue fibrosis in many organs results from altered and excessive extracellular**
23 **matrix (ECM) protein deposition [1]. Concomitant with ECM expansion, resident lipid-**
24 **filled cells including mature adipocytes are lost in human and mouse fibrosis[2-5],**
25 **yet the mechanisms that drive mature adipocyte lipid loss and their contribution to**
26 **tissue fibrosis are unknown. Here, we identify an early, fibro-protective role of**
27 **mature adipocyte lipolysis driven by Wnt signaling during fibrosis onset. Using**
28 **chemical and genetic mouse models of skin fibrosis, we show that fibrotic stimuli**
29 **induce and maintain lipolysis in mature dermal adipocytes. Loss of the lipolytic**
30 **rate-limiting enzyme adipocyte triglyceride lipase (ATGL)[6,7] in murine dermal**
31 **adipocytes exacerbates bleomycin-induced fibrosis development. Adipocyte**
32 **lipolysis is stimulated in the early stages of Wnt signaling-induced skin fibrosis**
33 **and by Wnt agonists *in vitro.* Furthermore, deletion or inhibition of the Wnt target**
34 **gene, CD26/Dipeptidyl peptidase 4 (DPP4) prevented Wnt-induced lipolysis and**
35 **skin fibrosis in mice. Notably, DPP4 expression correlates with skin fibrosis**
36 **severity in human patients. Thus, we propose that adipocyte-derived fatty acids**
37 **and the Wnt-DPP4 axis act as essential regulators of ECM homeostasis within**
38 **tissues and provide a therapeutic avenue to manipulate fibrosis.**

40 Excessive deposition of ECM proteins leads to scarring or fibrosis, inducing tissue
41 stiffening and loss of function in virtually all organ systems, including the skin, adipose
42 tissue, heart, intestine, and lung[1]. Despite its devastating impact on nearly 5% of people
43 worldwide annually[8], no effective treatment for fibrosis exists. Interestingly, fibrosis occurs
44 concomitantly with a loss of lipid-filled cells in several organs including mature adipocytes
45 in the skin and lipo-fibroblasts in the lung and liver[2-5].

47 In the skin, adipocytes compose a distinct layer of dermal white adipose tissue (DWAT)
48 under the skin's ECM-rich dermal layers, making the skin an excellent system in which to
49 study how lipid-filled cells impact fibrosis development. Accumulation and breakdown of
50 lipids in adipocytes are regulated by the tightly controlled balance between *de novo*
51 lipogenesis, uptake, and breakdown of lipids including lipolysis, lipophagy, and exosomal
52 release of intact lipid[9-11] (Extended data FigS1.1). We and others have shown that a
53 subset of mature adipocytes undergo dedifferentiation and form myofibroblasts after
54 injury and in bleomycin-induced skin fibrosis in mice[12,13]. In skin repair, this fate transition
55 requires lipolysis and loss of lipid droplets in mature adipocytes in an adipocyte
56 triglyceride lipase (*Atgl*)-dependent manner[14]. However, the role of fatty acids, a product
57 of lipolysis, in fibrosis is unclear. While fatty acids can exacerbate lung fibrosis[15] and
58 systemic inhibition of lipolysis without fibrotic stimuli can modestly increase homeostatic
59 dermal ECM[16], fatty acids reduce ECM gene expression in preadipocyte 3T3 L1 cells *in*
60 *vitro*[17,18]. Together, these studies illustrate the need to better understand the role of
61 lipolysis in initiating and perpetuating fibrosis.

63 One potential regulator of adipocyte biology during fibrosis is the Wnt signaling pathway.
64 Canonical Wnt signaling through the stabilization of its transducer, β-catenin, drives tissue
65 fibrosis in many organs, including skin[19-21]. Wnt signaling can impact multiple aspects of
66 fibroblast biology including specification, proliferation, migration, myofibroblast formation,
67 and ECM production[22-24], all of which impact fibrosis pathogenesis. While Wnt signaling

68 can repress adipogenesis[25-28], the impact of Wnt signaling on mature adipocytes during
69 fibrosis is not known.

70

71 **Depletion of lipid from the dermal adipocyte layer is an early event in skin fibrosis:**
72 To explore the timing of fibrotic fat loss, skin fibrosis was induced by subcutaneous
73 injection of bleomycin in 6-8 week old mice[29]. While most skin fibrosis models analyze
74 fibrosis induction after 14-21 days, we detected ECM expansion and a 3-fold reduction in
75 Perlipin1+ (PLIN+) lipid droplet size in mature adipocytes within 5 days of bleomycin
76 treatment (Fig. 1a, b). Lineage tracing of mature adipocytes by tamoxifen-inducible
77 *AdiponectinCreER: mT/mG* reporter[30] revealed that, following bleomycin injection, GFP+
78 adipocytes remain in the DWAT region in early stages of fibrosis development, but display
79 smaller or absent PLIN+ vesicles (Fig. 1c, Extended data Fig.S1). Examination of dermal
80 adipocytes by electron microscopy[31] revealed unilocular lipid droplets in control skin
81 whereas bleomycin-injected skin contained adipocytes with multiple smaller lipid droplets
82 (Fig.1d). These data indicate that loss of lipid occurs during skin fibrosis onset, prompting
83 us to confirm whether this was due to lipolysis.

84

85 **Inhibition of adipocyte lipolysis exacerbates skin fibrosis development:**
86 To test the functional role of adipocyte lipolysis during fibrosis development, we examined
87 mice that specifically lack *Atgl/Pnpla2* in dermal adipocytes[6,7]. Deletion of *Atgl* using
88 *Adiponectin-CreER* mice results in severe impairment of FA mobilization during
89 starvation[32] and after skin injury[14]. We induced skin-specific *Atgl* loss with topical
90 tamoxifen treatment[14] and subsequently injected mice with bleomycin subcutaneously to
91 trigger skin fibrosis. Bleomycin-injected control (*CreER-*) mice displayed reduced dermal
92 white adipose tissue (DWAT), however, tamoxifen and bleomycin-injected *Adiponectin-*
93 *CreER; Atgl$^{fl/fl}$* mice retained their DWAT and lipid content (Fig. 2a, b, d). Electron
94 microscopy of dermal adipocytes confirmed unilocular lipid droplets in bleomycin-injected
95 *Adiponectin-CreER; Atgl$^{fl/fl}$* (Fig. 2d). Despite retaining dermal adipocyte size and lipid
96 storage, bleomycin-treated *Adiponectin-CreER; Atgl$^{fl/fl}$* mice displayed precocious dermal
97 thickening (Fig. 2a, b). To explore ECM remodeling in the skin of these mice, we analyzed
98 the levels of unfolded collagen chains using fluorescent collagen hybridizing protein
99 (CHP) in the dorsal skin[33] (Fig. 2c). We detected increased collagen remodeling
100 throughout the dermis of tamoxifen and bleomycin-treated *Adiponectin-CreER; Atgl$^{fl/fl}$*
101 mice compared to bleomycin-injected control mice (Fig. 2c). Together, these data reveal
102 that *Atgl*-dependent adipocyte lipolysis occurs in the early stages of fibrosis and that the
103 early activation of lipolysis during skin fibrosis inhibits ECM expansion during fibrosis
104 induction (Extended data S4.5).

105

106 **The lipolysis axis is stimulated by Wnt signaling in adipocytes**
107 Because Wnt/β-catenin signaling has a key role in fibrosis[19-21,34] and can impact
108 adipocyte differentiation[25-28], we analyzed whether Wnt signaling stimulates the lipolytic
109 pathway in skin fibrosis. We induced the expression of stabilized β-catenin, the signal
110 transducer of activated canonical Wnt signaling, in *Engrailed1+(En1)* dermal fibroblasts
111 and adipocyte stem cells[13,22,35] using *En1Cre/+; R26rtTA/+; TetO-β-catenin/+* (β-cat^{istab})
112 mice (Fig 3a, Extended data Fig. S3.1, S4.3). Dietary doxycycline induced β-cat^{istab}
113 resulted in significant ECM expansion in the dermis and marked DWAT reduction within

114   10 days (Fig. 3a). β-cat[istab] throughout the dermis leads to a reduction in DWAT layer
115   thickness (Fig. 3a) and reduced size of individual PLIN[+] droplets within adipocytes (Fig
116   3b), despite sustained hair follicle growth (Extended data Fig. S4.3) and associated hair
117   adipocyte enlargement[36]. Interestingly, subsequent withdrawal of doxycycline in β-cat[istab]
118   for 3 weeks led to rescue of DWAT and dermal thickness (Fig. 3a). Thus, the depletion of
119   lipid within mature dermal adipocytes in mouse skin fibrosis is Wnt signaling-dependent
120   and reversible.
121
122   Next, we examined whether activation of canonical Wnt signaling could induce adipocyte
123   lipolysis by analyzing phosphorylation of Hormone Sensitive Lipase (pHSL) and
124   Perilipin[37] and glycerol release, an end stage product specific to the lipolysis pathway
125   (Extended data Fig. S1.1). β-cat[istab] stimulated a nearly two-fold increase in pHSL in β-
126   cat[istab] skin after 5 days, preceding visible lipid depletion (Fig. 3c). Greater numbers of
127   phospho-Perilipin[+] adipocytes were also detected (Extended data Fig. S4.3). Electron
128   microscopy confirmed that β-cat[istab]-expressing skin had numerous small intracellular lipid
129   droplets in DWAT adipocytes (Fig. 3d), confirming that lipid dynamics are altered upon
130   Wnt activation. Further, treatment with the Wnt agonist CHIR99021 induced adipocyte
131   lipid loss *in vitro*. Using Oil Red O staining to label lipid content, we observed that
132   treatment of 3T3-L1 differentiated adipocytes and primary mouse dermal adipocytes with
133   CHIR99021 induced loss of lipid in cultured adipocytes (Fig. 3e and Extended data S4.4).
134   Visible lipid depletion was preceded by elevated free glycerol in media, indicating that
135   lipolysis is induced by Wnt activation (Fig. 3e). Glycerol release was abrogated in
136   CHIR99021 treated cells in the presence of an ATGL inhibitor, atglistatin (Fig. 3e),
137   indicating that reduction in lipid content is due to ATGL-dependent lipolysis. Collectively,
138   these data suggest that lipolysis is activated by Wnt signaling and drives lipid loss during
139   the onset of skin fibrosis (Extended data S4.5).
140
141   **Wnt-induced DPP4/CD26 is necessary for lipid depletion of dermal adipocytes.**
142   To better understand the mechanisms by which Wnt/β-cat signaling promotes fibrosis and
143   adipocyte lipolysis, we analyzed the transcriptome of β-cat[istab] dermal fibroblasts (GSE
144   103870)[38]. DPP4 was one of 10 most differentially expressed genes and was highly
145   upregulated (47x, p≤0.005) in β-cat[istab] dermal fibroblasts[38]. The expression of DPP4 was
146   of particular interest because it is expressed in fibrotic fibroblasts[13] and its inhibition
147   affects ECM accumulation in injury models[35,39] and only partially protects from ECM
148   accumulation chemical models of fibrosis[40], although its role in lipid handling is unknown.
149   DPP4 immunoreactivity was increased in human systemic sclerosis (SSc) and keloids,
150   correlating with SSc disease severity compared to control human skin (Fig. 4a and
151   Extended data Fig. S4.1). Wnt activation induced *Dpp4* mRNA expression in β-cat[istab]
152   fibroblasts and CHIR99021-treated mouse primary dermal adipocytes *in vitro* (Extended
153   data Fig. S4.2)*. DPP4 protein is increased in β-cat[istab] dermis and DWAT *in vivo* and in
154   bleomycin-injected skin (Fig. 4b and Extended data Fig. S4.2). After reversal from β-
155   cat[istab], *Dpp4* mRNA and DPP4 protein expression levels were restored to control levels
156   *in vitro* and *in vivo*, respectively (Extended data Fig. S4.2). Together, these data
157   demonstrate that DPP4 expression is responsive to Wnt signaling in both dermal
158   fibroblasts and adipocytes.
159

160 Next, we tested if DPP4 inhibition (DPP4$_i$) accelerates recovery from Wnt-induced dermal
161 fibrosis. During early reversal caused by withdrawal of dietary doxycycline for 10 days, β-
162 cat^{istab} skin remained fibrotic and DWAT remained depleted. Treatment of β-cat^{istab} skin
163 during the first 10 days of the reversal phase with a DPP4 inhibitor, sitagliptin, accelerated
164 the recovery of DWAT and dermal thickness (Fig. 4c). *In vitro*, sitagliptin treatment also
165 partially rescued ORO+ lipid droplets in CHIR99021 treated mature adipocytes (Extended
166 data Fig. S4.4). However, sitagliptin co-treatment with CHIR99021 did not fully rescue
167 Wnt-stimulated lipolysis *in vitro*, suggesting that DPP4 function in adipocytes is also likely
168 mediated in part by membrane bound DPP4/CD26, which is not targeted by inhibitors or
169 additional Wnt targets are involved (Fig. 4g).
170
171 Subsequently, we tested the hypothesis that Wnt-induced *Dpp4* expression controls
172 adipocyte lipolysis and ECM accumulation *in vivo* by examining whether genetic deletion
173 of *Dpp4* rescues Wnt-induced fibrosis phenotypes. First, we confirmed that Wnt signaling
174 is activated in the dermis and DWAT of *Dpp4*$^{-/-}$; β-cat^{istab} mice and indeed, we detected
175 nuclear β-catenin in both *Dpp4*$^{+/+}$ and *Dpp4*$^{-/-}$; β-cat^{istab} mice (Extended Data Fig. S4.3).
176 Strikingly, *Dpp4*$^{-/-}$; β-cat^{istab} mice displayed a marked preservation of DWAT, increased
177 PLIN$^+$ lipid droplet size, attenuated dermal thickening, in comparison to *Dpp4*$^{+/+}$; β-cat^{istab}
178 mice (Fig. 4D and E). Collagen remodeling was significantly diminished in the DWAT and
179 lower dermal regions in *Dpp4*$^{-/-}$; β-cat^{istab} (Fig. 4e, Extended Data Fig. S4.3). There was
180 attenuated expression of p-Perilipin and electron microscopy revealed intact unilocular
181 lipid droplets in *Dpp4*$^{-/-}$; β-cat^{istab} compared to *Dpp4*$^{+/+}$;β-cat^{istab} dermal adipocytes,
182 demonstrating protection from lipolysis (Fig. 4e, 4f, Extended data Fig. S4.3,). Taken
183 together, these data indicate that DPP4 is required for Wnt-induced adipocyte lipolysis
184 and ECM expansion during fibrosis onset and DPP4$_i$ can accelerate the recovery from
185 established Wnt-induced fibrosis. These findings resonate with recent work linking DPP4
186 with obesity, metabolic syndrome, adipocyte dedifferentiation *in vitro,* inhibition of
187 adipocyte differentiation *in vivo*[41-43], scar formation[13,35], and fibrosis[39,40,44].
188
189 **Discussion**
190 By combining chemical and genetic models of skin fibrosis development with genetic and
191 pharmacological manipulations (Fig. 4g, Extended data Fig. S4.5), our data unearth
192 molecular mechanisms that drive adipocyte lipolysis and govern ECM homeostasis during
193 fibrosis development. Given the presence of mature adipocytes in the heart and kidney
194 stroma and lipofibroblasts in the lung [2-5], the Wnt-Dpp4-adipocyte axis may explain the
195 crucial role of Wnt signaling in concert with other fibrotic stimuli in fibrogenesis of the
196 several other tissues[45]. Furthermore, since fatty acid metabolism[46], lipid loss[47,48], and
197 fibroblast activation accompany tumor growth and metastasis[35], our data may shed light
198 on key mechanisms that impact tissue morphogenetic changes in many disease states.
199
200 Our findings also resonate with recent reports that heterogeneous fibroblast populations
201 express DPP4 during skin homeostasis and repair[35,49,50] and DPPs' peptidase activity
202 plays a crucial role for inflammation, wound repair, and tumorigenesis[13,51,52]. Together,
203 our data further demonstrate that DPP4 regulates both homeostasis of adipocyte lipid
204 content and fibroblast ECM production to impact tissue fibrosis and promote recovery.
205 We propose that DPP4's broad substrate repertoire including chemokines and metabolic

206   regulators may drive multiple aspects of fibrosis development and that FDA-approved
207   DPP4 inhibitors may be useful to accelerate clinical treatments for fibrosis prevention
208   and/or recovery.
209
225
226   **Author Contributions:** V.H., A.J., E.C. and R.P.A conceived the experimental plan.
227   V.H, R.P.A, A.J., V.L. and E.C. performed the experiments, made the figures, and did the
228   analysis. M.S., E.H-S., S.K., B.Z. and V.L. contributed to data collection. S.K. and B.Z
229   developed and performed machine learning algorithms for quantitative image analysis.
230   J.L, Y.Y., R. L. and S.R. contributed key mouse reagents and human samples.
231
236
237   **Materials and Correspondence:** Valerie Horsley: Valerie.horsley@yale.edu   and
238   Radhika Atit: rpa5@case.edu
239
240
241

References

1. Distler, J. H. W. *et al.* Shared and distinct mechanisms of fibrosis. *Nature Reviews Rheumatology* **15,** 705–730 (2019).

2. Agha, El, E. *et al.* Two-Way Conversion between Lipogenic and Myogenic Fibroblastic Phenotypes Marks the Progression and Resolution of Lung Fibrosis. *Cell Stem Cell* **20,** 261–273.e3 (2017).

3. Rehan, V. K. & Torday, J. S. The lung alveolar lipofibroblast: an evolutionary strategy against neonatal hyperoxic lung injury. *Antioxidants & redox signaling* **21,** 1893–1904 (2014).

4. Schmidt, B. A. & Horsley, V. Intradermal adipocytes mediate fibroblast recruitment during skin wound healing. *Development* **140,** 1517–1527 (2013).

5. Hernandez-Gea, V. & Friedman, S. L. Pathogenesis of liver fibrosis. *Annu Rev Pathol* **6,** 425–456 (2011).

6. Haemmerle, G. *et al.* Defective lipolysis and altered energy metabolism in mice lacking adipose triglyceride lipase. *Science* **312,** 734–737 (2006).

7. Fischer, J. *et al.* The gene encoding adipose triglyceride lipase (PNPLA2) is mutated in neutral lipid storage disease with myopathy. *Nat Genet* **39,** 28–30 (2007).

8. Zhao, X., Kwan, J. Y. Y., Yip, K., Liu, P. P. & Liu, F.-F. Targeting metabolic dysregulation for fibrosis therapy. *Nat Rev Drug Discov* **19,** 57–75 (2020).

9. Flaherty, S. E. *et al.* A lipase-independent pathway of lipid release and immune modulation by adipocytes. *Science* **363,** 989–993 (2019).

10. Cingolani, F. & Czaja, M. J. Regulation and Functions of Autophagic Lipolysis. *Trends Endocrinol. Metab.* **27,** 696–705 (2016).

11. Frühbeck, G., Méndez-Giménez, L., Fernández-Formoso, J.-A., Fernández, S. & Rodríguez, A. Regulation of adipocyte lipolysis. *Nutr Res Rev* **27,** 63–93 (2014).

12. Marangoni, R. G. *et al.* Myofibroblasts in Murine Cutaneous Fibrosis Originate From Adiponectin-Positive Intradermal Progenitors. *Arthritis & Rheumatology* **67,** 1062–1073 (2015).

13. Shook, B. A. *et al.* Myofibroblast proliferation and heterogeneity are supported by macrophages during skin repair. *Science* **362,** eaar2971 (2018).

14. Shook, B. A. *et al.* Dermal Adipocyte Lipolysis and Myofibroblast Conversion Are Required for Efficient Skin Repair. *Cell Stem Cell* **26,** 880–895.e6 (2020).

15. McManus, B. & Knight, D. Long-chain fatty acids are bad in IPF, or are they? *Respirology* **50,** 122 (2020).

16. Zhang, Z. *et al.* Dermal adipocytes contribute to the metabolic regulation of dermal fibroblasts. *Exp Dermatol* **30,** 102–111 (2021).

17. Ezure, T. & Amano, S. Negative Regulation of Dermal Fibroblasts by Enlarged Adipocytes through Release of Free Fatty Acids. *Journal of Investigative Dermatology* **131,** 2004–2009 (2011).

18. Zhao, X. *et al.* Metabolic regulation of dermal fibroblasts contributes to skin extracellular matrix homeostasis and fibrosis. *Nature Metabolism* 1–15 (2019). doi:10.1038/s42255-018-0008-5

19. Hamburg-Shields, E., DiNuoscio, G. J., Mullin, N. K., Lafayatis, R. & Atit, R. P. Sustained β-catenin activity in dermal fibroblasts promotes fibrosis by up-regulating expression of extracellular matrix protein-coding genes. *J. Pathol.* **235,** 686–697 (2015).

20. Akhmetshina, A. *et al.* Activation of canonical Wnt signalling is required for TGF-β-mediated fibrosis. *Nature Communications* **3,** 735–12 (2012).

21. Hu, H.-H., Cao, G., Wu, X.-Q., Vaziri, N. D. & Zhao, Y.-Y. Wnt signaling pathway in aging-related tissue fibrosis and therapies. *Ageing Res Rev* **60,** 101063 (2020).

22. Atit, R. *et al.* Beta-catenin activation is necessary and sufficient to specify the dorsal dermal fate in the mouse. *Developmental Biology* **296,** 164–176 (2006).

23. Cheon, S. S. *et al.* beta-Catenin stabilization dysregulates mesenchymal cell proliferation, motility, and invasiveness and causes aggressive fibromatosis and hyperplastic cutaneous wounds. *Proc Natl Acad Sci USA* **99,** 6973–6978 (2002).

24. Sharma, M. & Pruitt, K. Wnt Pathway: An Integral Hub for Developmental and Oncogenic Signaling Networks. *Int J Mol Sci* **21,** 8018 (2020).

25. Prestwich, T. C. & MacDougald, O. A. Wnt/beta-catenin signaling in adipogenesis and metabolism. *Current Opinion in Cell Biology* **19,** 612–617 (2007).

26. Choy, L., Skillington, J., biology, R. D. T. J. O. C.2000. Roles of autocrine TGF-β receptor and Smad signaling in adipocyte differentiation. *Journal of Cell Biology* **149,** 667–682 (2000).

27. Clouthier, D. E., Comerford, S. A. & Hammer, R. E. Hepatic fibrosis, glomerulosclerosis, and a lipodystrophy-like syndrome in PEPCK-TGF-beta1 transgenic mice. *J. Clin. Invest.* **100,** 2697–2713 (1997).

28. Zeve, D. *et al.* Wnt signaling activation in adipose progenitors promotes insulin-independent muscle glucose uptake. *Cell Metab.* **15,** 492–504 (2012).

29. Takagawa, S. *et al.* Sustained activation of fibroblast transforming growth factor-beta/Smad signaling in a murine model of scleroderma. *J Invest Dermatol* **121,** 41–50 (2003).

30. Rivera-Gonzalez, G. C. *et al.* Skin Adipocyte Stem Cell Self-Renewal Is Regulated by a PDGFA/AKT-Signaling Axis. *Cell Stem Cell* **19,** 738–751 (2016).

31. Zwick, R. K. *et al.* Adipocyte hypertrophy and lipid dynamics underlie mammary gland remodeling after lactation. *Nature Communications* **9,** 3592 (2018).

32. Zechner, R., Kienesberger, P. C., Haemmerle, G., Zimmermann, R. & Lass, A. Adipose triglyceride lipase and the lipolytic catabolism of cellular fat stores. *J. Lipid Res.* **50,** 3–21 (2009).

332   33.   Hwang, J. *et al.* In Situ Imaging of Tissue Remodeling with Collagen
333   Hybridizing Peptides. *ACS Nano* **11,** 9825–9835 (2017).
334   34.   Mastrogiannaki, M. *et al.* β-Catenin Stabilization in Skin Fibroblasts Causes
335   Fibrotic Lesions by Preventing Adipocyte Differentiation of theReticular
336   Dermis. *J Invest Dermatol* **136,** 1130–1142 (2016).
337   35.   Rinkevich, Y. *et al.* Identification and isolation of a dermal lineage with
338   intrinsic fibrogenic potential. *Science* **348,** aaa2151–aaa2151 (2015).
339   36.   Festa, E. *et al.* Adipocyte lineage cells contribute to the skin stem cell niche
340   to drive hair cycling. *Cell* **146,** 761–771 (2011).
341   37.   McDonough, P. M. *et al.* Differential phosphorylation of perilipin 1A at the
342   initiation of lipolysis revealed by novel monoclonal antibodies and high
343   content analysis. *PLoS ONE* **8,** e55511 (2013).
344   38.   Mullin, N. K. *et al.* Wnt/β-catenin Signaling Pathway Regulates Specific
345   lncRNAs That Impact Dermal Fibroblasts and Skin Fibrosis. *Front Genet* **8,**
346   183 (2017).
347   39.   Wang, X. M. *et al.* The pro-fibrotic role of dipeptidyl peptidase 4 in carbon
348   tetrachloride-induced experimental liver injury. *Immunol Cell Biol* **95,** 443–
349   453 (2017).
350   40.   Soare, A. *et al.* Dipeptidylpeptidase 4 as a Marker of Activated Fibroblasts
351   and a Potential Target for the Treatment of Fibrosis in Systemic Sclerosis.
352   *Arthritis Rheumatol* **72,** 137–149 (2020).
353   41.   Lamers, D. *et al.* Dipeptidyl Peptidase 4 Is a Novel Adipokine Potentially
354   Linking Obesity to the Metabolic Syndrome. **60,** 1917–1925 (2011).
355   42.   Bouchard, L. *et al.* Comprehensive genetic analysis of the dipeptidyl
356   peptidase-4 gene and cardiovascular disease risk factors in obese
357   individuals. *Acta Diabetol* **46,** 13–21 (2009).
358   43.   Lessard, J. *et al.* Characterization of Dedifferentiating Human Mature
359   Adipocytes from the Visceral and Subcutaneous Fat Compartments:
360   Fibroblast-Activation Protein Alpha and Dipeptidyl Peptidase 4 as Major
361   Components of Matrix Remodeling. *PLoS ONE* **10,** e0122065 (2015).
362   44.   Hu, M. S. & Longaker, M. T. Dipeptidyl Peptidase-4, Wound Healing,
363   Scarring, and Fibrosis. *Plastic and Reconstructive Surgery* **138,** 1026–1031
364   (2016).
365   45.   Piersma, B., Bank, R. A. & Boersema, M. Signaling in Fibrosis: TGF-β,
366   WNT, and YAP/TAZ Converge. *Front Med (Lausanne)* **2,** 59 (2015).
367   46.   Pascual, G. *et al.* Targeting metastasis-initiating cells through the fatty acid
368   receptor CD36. *Nature Publishing Group* 1–25 (2016).
369   doi:10.1038/nature20791
370   47.   Nieman, K. M. *et al.* Adipocytes promote ovarian cancer metastasis and
371   provide energy for rapid tumor growth. *Nat Med* **17,** 1498–1503 (2011).
372   48.   Zhang, M. *et al.* Adipocyte-Derived Lipids Mediate Melanoma Progression
373   via FATP Proteins. *Cancer Discov* **8,** 1006–1025 (2018).
374   49.   Tabib, T., Morse, C., Wang, T., Chen, W. & Lafyatis, R. SFRP2/DPP4 and
375   FMO1/LSP1 Define Major Fibroblast Populations in Human Skin. *J Invest*
376   *Dermatol* **138,** 802–810 (2018).

377   50.   Merrick, D. *et al.* Identification of a mesenchymal progenitor cell hierarchy in
378   adipose tissue. *Science* **364,** eaav2501–13 (2019).
379   51.   Baticic Pucar, L., Pernjak Pugel, E., Detel, D. & Varljen, J. Involvement of
380   DPP IV/CD26 in cutaneous wound healing process in mice. *Wound Repair*
381   *Regen* **25,** 25–40 (2017).
382   52.   Driskell, R. R. *et al.* Distinct fibroblast lineages determine dermal
383   architecture in skin development and repair. *Nature* **504,** 277–281 (2013).
384

385
386
387 **Methods:**
388 **Mouse handling and lines**
389 *Engrailed1Cre (En1Cre)*[53]; *Rosa26rTA-EGFP*[54] (Jax Stock 005572) ; *TetO-deltaN89 β-*
390 *catenin*[55]; *Dpp4*[-/-56]; *Adiponectin Cre-ER*[T2 57] (Jax stock 025124); *Atgl* flox[58] (Jax stock
391 024278); Rosa26 mTmG reporter[59] (Jax stock 007676) lines were genotyped as
392 previously described. The contribution of the *En1Cre* lineage cells in the skin has been
393 previously described[13,22,35,60] . For induction of *TetO-deltaN89 β-catenin-myc* tagged
394 transgene expression in the *En1Cre;R26rtTA* recombined cells, 21-day old (P21) triple
395 transgenic mice were given 6g/kg of dietary doxycycline in rodent chow (Envigo-Harlan)
396 and 2mg/ml doxycycline in water (Sigma) for three weeks. For induction-reversible
397 experiments, P21 mice were first treated with dietary doxycycline until P42 and then
398 switched to regular chow and water. At desired time points, mice were euthanized and
399 dorsal skin was processed for frozen or paraffin sections as previously described[22]. For
400 each experiment, mutants with litter-matched controls were studied. At least two to four
401 litters were used for phenotypic analysis.
402 Lineage marking of mature adipocytes was achieved using tamoxifen inducible
403 *Adiponectin Cre-ER; Rosa26mTmG* reporter. Topical tamoxifen of 5mg/mL in 100%
404 ethanol is painted directly on the shaved dorsal skin two days prior to bleomycin injection.
405 Conditional deletion of *Atgl/Pnlap2 in mature adipocytes* was done in *Adiponectin Cre-*
406 *ER; Rosa26mTmG; Atgl*[flox/flox] and verified as previously described[14] Fibrosis was induced
407 between 6-8 weeks of age in either wild-type or *Adiponectin Cre-ER; Rosa26mTmG;*
408 *Atgl*[flox/flox] males of C57Bl/6 in bred background. Littermate Cre-negative controls were
409 used for the experiments. Mice are then given daily subcutaneous injection on their upper
410 dorsal region with 300µg of Bleomycin Sulfate (Enzo pharmaceuticals BML-AP302-0010)
411 in 100µL PBS for 3, 5 or 11 days. Bleomycin experiments were done on C57Bl/6 male
412 mice to avoid confounding sexual maturity related differences[61]. Vials of bleomycin sulfate
413 were checked for efficacy prior to experimental treatments. To ensure injections are
414 located to a 0.5in x 0.5 in square, mice are placed under light isoflurane anesthesia prior
415 to injections. 24 hours after the final injection, mice are euthanized and the dorsal skin is
416 collected.
417
418 Yale University and Case Western Reserve Institutional Animal Care and Use Committee
419 approved all animal procedures in accordance with AVMA guidelines Protocol 2013-0156,
420 approved 21 November 2014, Animal Welfare Assurance No. A3145-01 at Case Western
421 and Protocol 11248 #A3230-01Yale University.

422 **Patient Skin samples:** Samples were obtained by performing 3 mm punch biopsies from
423 the dorsal mid-forearm of healthy control and systemic sclerosis (SSc) human subjects
424 after informed consent under a protocol approved by the University of Pittsburgh
425 Institutional Review Board. Archived de-identified patient SSc skin samples with Modified
426 Rodnan Skin score (MRSS) were obtained from Scleroderma Center of Research
427 Translation. For human tissue immunohistochemistry, access to archived de-identified
428 keloid tissue was in compliance with the Case Western Reserve University Institutional
429 Review Board for Human Studies.

Adipocyte cell culture

All data were obtained from primary dermal adipocyte progenitors isolated from wild-type CD1 background P4 dorsal skin. Approximately 1cm^2 dorsal skin was removed, rinsed in sterile 1x phosphate buffered saline (PBS), minced, and placed in 2mg/mL collagenase (Worthington, LS004196) with 2% bovine serum albumin (BSA) (Fisher, BP1600) and incubated in a 37ºC rotating incubator for 45 minutes. Digested skin was filtered through a 70μM cell strainer (cat number) and plated in 60mm tissue culture plastic plates. Cells were passaged 2-3 times when they achieved approximately 80% confluence. Adipocyte differentiation was stimulated with adipocyte induction media (AIM) (DMEM (Thermofisher, 11995065) containing glucose, pyruvate, 10% fetal bovine serum (FBS), 100μM indomethacin, 1μM dexamethasone, 500μM 3-isobutyl-1-methylxanathine (IBMX), and 10μM insulin) for 8-12 days. Duplicate cultures were kept in media containing only glucose and pyruvate. Differentiated adipocytes were enriched by trypsinizing (0.25% Trypsin EDTA (Thermofisher: 25200056)) and re-plating on a 12-well plate for treatment. Some differentiated adipocytes were kept in maintenance media only (DMEM with glucose, pyruvate, FBS, and insulin), or with additives such as 7μM CHIR (Cayman, 13122), 40μM atglistatin (Sigma Aldrich, SML1075-5MG), and/or 20μM sitagliptin (Cayman, 13252). All media was prepared fresh and changed every 2nd day. Following 4 days of treatment, media was collected from each well and free glycerol was quantified using Free Glycerol Reagent (Sigma-Aldrich F6428-40ML). Data was plotted relative to untreated control mature adipocytes from the same mouse and analyzed using a paired *t*-test with Welch's correction. Following 8 days of treatment cells were rinsed and fixed for 1 hour in 10% neutral buffered formalin. They were then stained with Oil Red O (ORO) (Sigma Aldrich, O0625-25G) for 10 minutes and rinsed with water before they were imaged on a Leica DMi8 inverted microscope. Camera positions within wells were held constant between plates and each well was photographed in 2 non-overlapping regions. Images were then quantified using Cell Profiler^{TM} (See below) to estimate coverage and average coverage per condition was displayed relative to untreated control cells and analyzed with a paired *t*-test with Welch's correction. Experiments were repeated on 3-4 biological replicates.

Histological staining and morphometrics

Dorsal mouse skin from mice of various ages (p26, p32, p42, p68) was isolated, fixed in 4% PFA, and equilibrated in 25% sucrose for cryosectioning. Dorsal back skin was isolated from 6-8-week-old mice. It was directly frozen in OCT for cryosectioning at 14 μm. Alternatively, dorsal skin pieces were drop-fixed 10% neutral buffered formalin for 1 hour at 4 degrees and then processed for paraffin sectioning at 7μm. Sections were stained with Masson's trichrome for mature Collagen I expression or hematoxylin and eosin according to standard protocols. Brightfield images were captured with an Olympus BX60 microscope and Cell Sens entry software and Zeiss AX10 scope and Zen 2.6 pro software. Dermal thickness, DWAT thickness, and adipocyte number were quantified with measurement tool in Fiji/Image J software. Data represent the average thickness in three different regions in 5-10 non-overlapping fields/mouse[12,19].

Immunohistochemistry and Immunofluorescence

For Figures 1 and 2 and Extended Data S1.1, frozen tissue was sectioned at a thickness of 14μM for immunofluorescence staining. Slides were fixed for 10 minutes in 4% paraformaldehyde (PFA) prior to staining. For Figures 3 and 4 and Extended data Fig 3.1, 4.1- 4.5, drop-fixed paraffin tissue was embedded and sectioned at 7μM. Paraffin sections were deparaffinized and washed with 1xPBS. They underwent antigen retrieval in citrate buffer (10 mM Tri-Sodium Citrate dyhydrate, 0.05% Tween-20, pH 6.0) for 15 minutes at 93ºC in a water bath. Following 10% normal goat serum block, with 0.05% Tween-20 or 0.3% Triton for 1 hr at room-temperature, tissue was incubated with appropriate primary antibody overnight at 4ºC. Primary antibodies for GFP (Abcam ab13970, 1:1000), β-Catenin (BD Biosciences, 1:250), myc-tag (Cell Signaling 7D10, 1:50), perilipin (Abcam ab3526, 1:500; Abcam ab61682, 1:500), p-perlipin1 (Vala Sciences, 4856), and CD26/DPP4 (Abcam ab28340, R&D: AF954) were used for brightfield immunohistochemistry or immunofluorescence as previously described[19,55,62]. After three washes in PBST (PBS+ 0.3% Triton or 0.05% Tween), species-appropriate secondary antibodies conjugated to biotin (Vector) or Alexa-fluor (Thermo-Fisher) were used. Nuclei were counterstained with hematoxylin or DAPI (1:2,000) before mounting in Fluoroshield (Sigma). Negative controls were used to confirm antibody specificity.

Imaging: Brightfield Images were takes at room temperature. Brightfield images in Figure 1 and 2 were obtained using Zeiss AX 10 upright scope equipped with a digital camera (Hamamatsu, ORCA-Flash4.0) and a 10x Objective (Zeiss Plan-APOCHROMAT). Brightfield images of Masson's Trichrome staining in Figure 3 and 4 and extended data E3.1, 3.2, 3.3 were taken using a Olympus BX60 microscope with a digital camera (DP70, Olympus) with Cell Sens Entry software (Ver. 1.5, © Olympus Corporation 2011) with a 4x objective (Olympus UPlanFI 4x/0.13) . Exposure was held constant between controls and experimental group. Brightfield images of Oil Red O stained cells in Fig. 3E and Extended data figure S4.4 were imaged on an inverted widefield Leica Dmi8 microscope with a digital camera and a 10x objective (HC PL FLUOTAR 40x/0.60, Dry, FWD=3.3-1.9mm).

Immunofluorescence images in Figure 1 and 2 and extended 1.1 were obtained on the Zeiss AX 10 upright scope equipped with a digital camera (Hamamatsu, ORCA-Flash4.0) and a 20x Objective (Zeiss Plan-APOCHROMAT). Immunofluorescence images in Figure 3B and 4E were imaged on an inverted confocal Leica TCS SP8 gated STED 3x microscope (DMI6000, Leica), using a 40x oil immersion objective (HC PL APO 40x/1.30 NA CS2, Oil, FWD=0.24 mm) detection by PMT detector and/or hybrid detectors and Leica LAS X software. CHP images were taken at 40x magnification on an inverted widefield Leica Dmi8 microscope. Max projections were generated and assembled using Fiji/ImageJ and analyzed in Cell Profiler. Images were processed and merged using Adobe Photoshop and laid out Adobe InDesign or Illustrator.

Image treatment and analysis.

Adipocyte perilipin+ cross-sectional area:

For Figure 1 and 2, 20x images on the Zeiss AX10 scope were analyzed. For Figure 3 and 4, 40X confocal images were analyzed in FIJI ImageJ. With FIJI's polygon selection

522 tool, at least 50 adipocytes were counted per mouse from non-overlapping fields. The
523 areas of these identified adipocytes were binned in a histogram generated in GraphPad
524 Prism.
525
526 Corrected total Perilipin fluorescence:
527 20x images of WT mice stained with Perilipin were analyzed using FIJI. The DWAT layer,
528 which contained perilipin was outlined. The area and perilipin fluorescence intensity were
529 measured. Three full-thickness fields of the dermis (perilipin negative) were measured for
530 fluorescent intensity to determine the average mean background fluorescence. Corrected
531 total fluorescence was measured as perilipin intensity - (area * average background).
532
533 ORO Pipeline:
534 Prior to feeding a batch of 4x images through the Cell Profiler^{TM} pipeline, an
535 undifferentiated control ORO image was first used for white-balancing using Adobe
536 Photoshop's image processor. The configurations of this white-balancing action were
537 input into a white-balancing script and the full batch of images were white balanced with
538 the script. Next, the images were loaded into Cell Profiler^{TM} and placed through an *Image*
539 *Math* module (Operation: Invert, Multiply the first image by: 1.5) to invert the image. The
540 inverted images were converted into grayscale images using a *Color To Gray* module
541 (Conversion method: Split) and split into RGB channels. Each of the 3 channels were run
542 through a series of *Correct Illumination Calculate* and *Correct Illumination Apply*
543 illumination correction modules. The grayscale "Green" and "Blue" channels were added
544 together in another *Image Math* module (Operation: Add) to more clearly show the ORO-
545 stained objects on a black background. An *Identify Primary Objects* module (Threshold
546 smoothing scale: 1.3488, Threshold correction factor: 1.0, Lower and upper bounds on
547 threshold: 0.0, 1.0, Size of adaptive window: 50) configured with an adaptive, 2-class
548 Otsu thresholding method was used to detect ORO-stained objects based on intensity.
549 Finally, a *Measure Image Area Occupied* module was used to output both the area
550 covered by ORO-stained objects as well as the total area of the image in squared pixels.
551
552 DPP4 Pipeline (SSc):
553 Prior to feeding a batch of 4x images through the Cell Profiler^{TM} pipeline, a human
554 forearm-skin DPP4 control image was first white-balanced using Photoshop's image
555 processor. The configurations of this white-balancing action were input into a white-
556 balancing script to be used on the entire batch. These white-balanced images were
557 loaded into Cell Profiler^{TM}. A *Crop* module was used to manually select a rectangular,
558 representative ROI in each image. Color deconvolution was completed using an *Unmix*
559 *Colors* module to separate the images into Hematoxylin and DAB channels. A *Reduce*
560 *Noise* module (Size: 7, Distance: 11, Cut-off distance: 0.045) was used on the DAB
561 channel. Unwanted objects including blood vessels and hair follicles were manually
562 identified through an *Identify Objects Manually* module. These identified objects were
563 transformed into a binary image via a *Convert Objects to Image* module. The area of
564 these unwanted objects was determined and recorded by a *Measure Image Area*
565 *Occupied* module. Using a *Mask Image* module (invert the mask: yes), a mask of the
566 unwanted objects was applied into the original ROI rectangle. The resulting ROI, with
567 unwanted objects masked out, was thresholded by a *Threshold* module via an adaptive,

568 3-class Otsu thresholding method in which the intermediate intensity objects were
569 classified as foreground objects (Threshold smoothing scale:0.0, Threshold correction
570 factor: 1.15, Lower and upper bounds on threshold: 0.15 & 1.0, Size of adaptive window:
571 50). The area of these threshold identified DPP4+ objects as well as the total ROI area
572 recorded by a *Measure Image Area Occupied* module. These recorded area data were
573 output by an *Export To Spreadsheet* module. The relevant total ROI area was determined
574 by subtracting the unwanted area from the total ROI area. The area covered by DPP4+
575 objects was divided by the relevant total ROI area to give the percent coverage of DPP4+
576 per image.
577
578 B-CHP pipeline: adapted from https://onlinelibrary.wiley.com/doi/pdf/10.1111/exd.13457
579 40X B-CHP images were loaded into Cell Profiler. Each original image was first split into
580 grayscale versions of its RGB channels using a *Color To Gray* module (Conversion
581 method: Split). An *Identify Objects Manually* module was used to trace and select an ROI
582 composed of the entire skin under the epidermis and above the panniculus carnosus. A
583 *Convert Objects To Image* module was used to convert the ROI into a binary image. A
584 *Closing* module (Structuring element shape, size: disk, 50) was applied to this binary ROI
585 to fill in any gaps left by the tracing performed in *Identify Objects Manually*. Using the
586 shape of this corrected binary ROI object, a sequence of *Morph* (performed operation:
587 distance) and *Image Math* modules are used to generate an intensity-based distance map
588 of the ROI based on distance from the epidermis. *Rescale Intensity* (Rescaling method:
589 Divide each image by the same value) modules then established how far down
590 subsequent layering modules would extend. Divisor values for *Rescale Intensity* modules
591 were changed for each image to the maximum thickness (pixel length) from the epidermis
592 to the panniculus carnosus. Using the epidermis distance map, *Threshold* modules
593 (Threshold strategy: global, thresholding method: manual, Threshold smoothing scale: 1,
594 Manual Threshold: increased from 0 to 1 in 0.05 increments), established binary regions
595 of increasing distance from the epidermis. *Image Math* modules (Operation: subtract)
596 were then used to subtract each thresholded binary region from the preceding region to
597 establish preliminary layers. This generated 20 preliminary layers spanning the ROI.
598 *Erode Image* modules (Structuring element shape, size: square, 10) were used to slightly
599 shrink each layer and ensure no overlap. An *Image Math* module (Operation: add) was
600 used to add eroded layers to produce a full map of the layers. A sequence of identification
601 and conversion modules was used to produce a binary image containing the area
602 occupied by the layers. Using an *Identify Objects Manually* layer, hair follicles and all area
603 including and under the *panniculus carnosus* were selected from the original B-CHP
604 image. Using a sequence of *Mask Image* and *Mask Objects* modules, these unwanted
605 objects were masked out of the binary image containing the area occupied by the layers.
606 This new masked binary image was composed of the area defined by the layers minus
607 the area of the unwanted objects. The new binary image was converted back into objects
608 using a *Convert Image To Objects* module. These objects were masked over the original
609 layers objects to generate the final map of the layers excluding unwanted areas. The red
610 intensity from the original red channel was then calculated per final layer using a *Measure
611 Object Intensity* module. A *Measure Object Size Shape* module was used to calculate the
612 area of each final layer. The final layers were then overlaid on the original image to ensure
613 correct functioning of the pipeline. The results were output using an *Export To
614 Spreadsheet* module.

Transmission Electron Microscopy analysis

Mice were anesthetized with ketamine and xylazine prior to perfusion. Mice were fixed by transcardial perfusion with 4% PFA according to standard protocols[31,63]. Samples were then submitted to the Yale EM core for processing and imaged as previously described[31]. Briefly, hardened blocks were cut using an ultramicrotome (UltraCut UC7; Leica). Ultrathin 60-nm sections were collected and stained using 2% uranyl acetate and lead citrate for transmission microscopy. Carbon-coated grids were viewed on a transmission electron microscope (Tecnai BioTWIN; FEI) at 80 kV. Images were taken using a CCD camera (Morada; Olympus) and iTEM (Olympus) software.

RNA extraction, and qRT-PCR analysis

Total RNA was extracted from cultured cells using Trizol reagent (Thermo Fisher: 15596026) and processed for qRT-PCR analysis with 4ng of cDNA as previously described {Hamburg-Shields:2015kd}. *Axin2* and *Dpp4* mRNA quantities were measured relative to *Hprt* using Taqman master mix (Thermofisher, 4304437) and probes (Thermofisher, Mm00443610_m1, Mm00494549_m1, Mm03024075_m1). Relative mRNA quantities were determined using an Applied Quantstudios Biosystems 3 PCR System. All samples were normalized to *Hprt* gene expression, and results are expressed as the fold change of Ct values relative to controls, using the $2-\Delta\Delta Ct$ formula. Complete qRT-PCR data was depicted in univariate scatter plots as recently described [64]. Statistical significance was determined by two-tailed, unpaired Student *t*-test with Welch's correction in GraphPad Prism software.

Western Blot analysis

Western blot was performed on flash frozen dorsal mouse skin samples. Samples were mechanically dismembrated, suspended in 1xRIPA buffer (Cell Signaling 9806S) and sonicated. 10-30μg protein was loaded per well. When stain free gel was used (pHSL blot), it was activated prior to transfer to PVDF membrane and total protein was detected before primary antibody incubation. Otherwise transfer to PVDF was performed without activation or total protein detection (DPP4 blot). Blots were incubated in 5% milk and 3% BSA block respectively for 1 hour at room temperature followed by incubation with α-DPP4 (R&D: AF954) or α-phospho-HSL (Cell signaling: 4139) primary antibody overnight at 4°C followed by species appropriate secondary antibody. Protein from stain-free blots (pHSL) were visualized on a Bio-Rad Chemidoc™ gel imager and data was graphed relative to total lane protein calculated in Image Lab software. Otherwise (DPP4), blot was developed on film, stripped, and re-probed with GAPDH loading control. Densitometry was calculated in Fiji and graphed relative to GAPDH loading control.

Statistical analysis

Sample size was determined based on published studies and no statistical method was employed. The experiments were not randomized. Due to the nature of the genetic manipulations, the authors were not blinded to allocation of animals for the experiments. The authors were blinded during results of the analyses. Individual data points on graphs represent the average value per mouse of 2-12 biological replicates (depending on measurement). Normality in the spread of data for each experiment was tested using Shapiro-Wilk test in GraphPad Prism software. Significance values for data sets

661 displaying normal distributions were calculated by unpaired Student *t*-test (two-tailed,
662 unequal variances) with Welch's correction in Prism software. Additionally, one-way
663 analysis of variance (ANOVA) was performed on Prism to compare dermal and DWAT
664 thickness between PBS control, BLM-Cre⁻ control and BLM *Atgl$^{fl/fl}$*. Paired t-tests are
665 performed where appropriate (*in vitro* only). Significance for non-normal distributed data
666 were calculated using the Mann-Whitney *U*-Test in Prism software. For graphs with
667 individual data points, each point represents the average of one mouse.   Error bars
668 represent standard error. All p values are included on the graphs and p values less than
669 0.05 are considered statistically significant.

671 **Data availability:** The data sets analyzed during the current study are available in the
672 GEO repository (GSE 103870).

674 **References for Methods section only**

675 53.   Kimmel, R. A. *et al.* Two lineage boundaries coordinate vertebrate apical
676   ectodermal ridge formation. *Genes & Development* **14,** 1377–1389 (2000).
677 54.   Belteki, G. *et al.* Conditional and inducible transgene expression in mice
678   through the combinatorial use of Cre-mediated recombination and
679   tetracycline induction. *Nucleic Acids Research* **33,** 1–10 (2005).
680 55.   Mukherjee, A. *et al.* A mouse transgenic approach to induce β-catenin
681   signaling in a temporally controlled manner. *Transgenic Res* **20,** 827–840
682   (2010).
683 56.   Marguet, D. *et al.* Enhanced insulin secretion and improved glucose
684   tolerance in mice lacking CD26. *Proc Natl Acad Sci USA* **97,** 6874–6879
685   (2000).
686 57.   Sassmann, A., Offermanns, S. & Wettschureck, N. Tamoxifen-inducible Cre-
687   mediated recombination in adipocytes. *genesis* **48,** 618–625 (2010).
688 58.   Sitnick, M. T. *et al.* Skeletal muscle triacylglycerol hydrolysis does not
689   influence metabolic complications of obesity. *Diabetes* **62,** 3350–3361
690   (2013).
691 59.   Muzumdar, M. D., Tasic, B., Miyamichi, K., Li, L. & Luo, L. A global double-
692   fluorescent Cre reporter mouse. *genesis* **45,** 593–605 (2007).
693 60.   Jiang, D. *et al.* Two succeeding fibroblastic lineages drive dermal
694   development and the transition from regeneration to scarring. *Nat Cell Biol*
695   **20,** 422–431 (2018).
696 61.   Azzi, L., El-Alfy, M., Martel, C. & Labrie, F. Gender differences in mouse skin
697   morphology and specific effects of sex steroids and
698   dehydroepiandrosterone. *J Invest Dermatol* **124,** 22–27 (2005).
699 62.   Myung, P. S., Takeo, M., Ito, M. & Atit, R. P. Epithelial Wnt Ligand Secretion
700   Is Required for Adult Hair Follicle Growth and Regeneration. *Journal of
701   Investigative Dermatology* **133,** 31–41 (2012).
702 63.   Xu, X. *et al.* Obesity activates a program of lysosomal-dependent lipid
703   metabolism in adipose tissue macrophages independently of classic
704   activation. *Cell Metab.* **18,** 816–830 (2013).

705   64.   Weissgerber, T. L., Milic, N. M., Winham, S. J. & Garovic, V. D. Beyond Bar
706   and Line Graphs: Time for a New Data Presentation Paradigm. *Plos Biol* **13,**
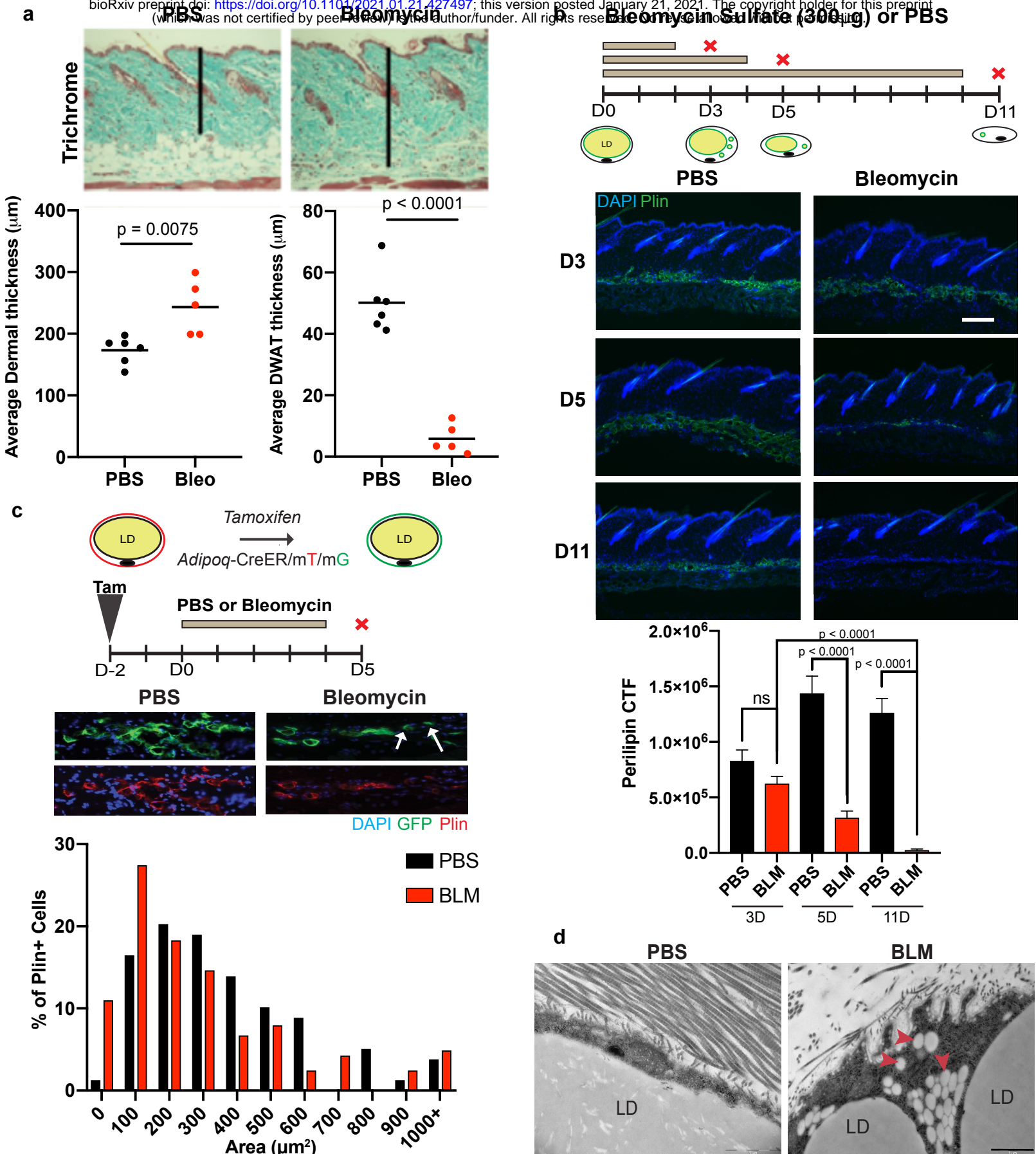707   e1002128 (2015).
708
709

Fig. 1: Adipocytes shrink during fibrosis development

a, Trichome stained skin sections of WT mice treated with vehicle (PBS) or bleomycin sulfate (BLM) after 5 days. Quantification of dermal and dermal white adipose tissue (DWAT) thickness in these mice. n=5-6 mice for each treatment. **b**, Representative images of perilipin (green) immunofluorescent staining of skin sections from WT mice treated with PBS or BLM for indicated days. Scale bar=200μm. Corrected total fluorescence (CTF) of perilipin immunostaining intensity during time course. n= 2-3 mice per bar. **c**, Genetic lineage tracing of dermal adipocytes in Adiponectin CreER; mTmG mice after 5 days of PBS or BLM treatment. Arrows indicate adipocytes lacking perilipin+ lipid droplets. Histogram of adipocyte size in mice treated with PBS or BLM treatment compared to PBS. **d**, Representative transmission electron microscopy (TEM) images of dermal adipocytes in PBS- and BLM-treated WT mice. LD=adipocyte lipid droplet. Arrowheads indicate lipid vesicles. Scale bar=1μm.
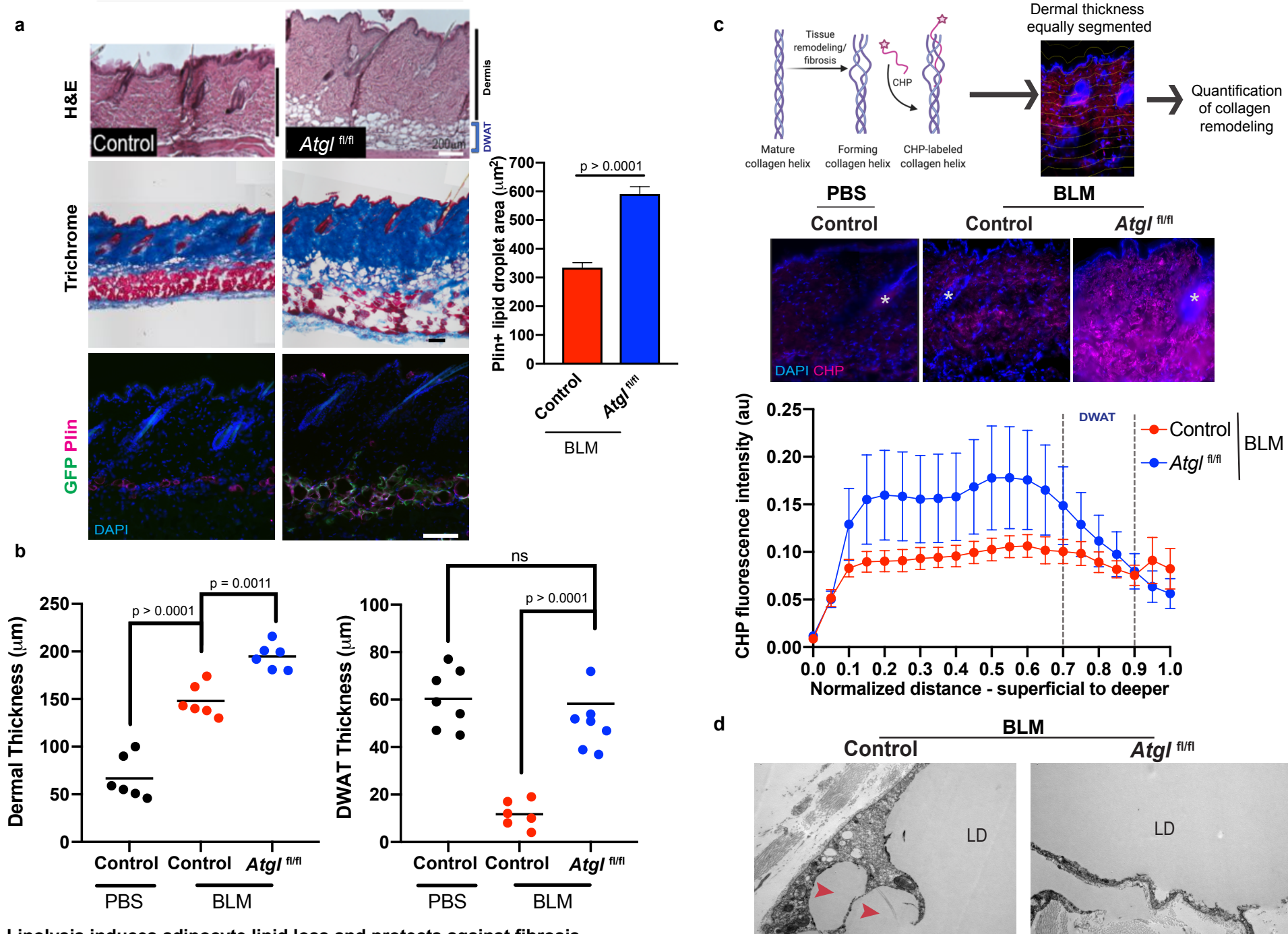
Fig. 2: Lipolysis induces adipocyte lipid loss and protects against fibrosis

a, Representative images and quantification of skin sections from control (Cre-) and Adiponectin CreER; mTmG; Atglfl/fl (Atglfl/fl) mice after 5 days of control or bleomycin (BLM) treatment stained with indicated dyes (Scale bar=200μm) or perilipin immunostaining (Scale bar=100m). Quantification of Perilipin+ (PLIN+) lipid droplets in control and Atglfl/fl mice. n = 5-7 mice for each genotype. **b**, Quantification of dermal and dermal white adipose tissue (DWAT) thickness in skin sections of control mice treated with PBS or BLM and Atglfl/fl mice treated with BLM. n=5-7 mice per genotype and treatment. **c**, Schematic of pipeline for analysis of collagen remodeling in skin sections. Representative images and quantification of collagen hybridizing peptide (CHP) fluorescent labelling of indicated genotypes and 5 days of control or BLM treatment. n= 3 mice for each treatment.
d, Representative TEM images of dermal adipocytes from BLM injected control and Atglfl/fl mice. LD=adipocyte lipid droplet. Arrowheads indicate lipid vesicles. Scale bar=2μm.

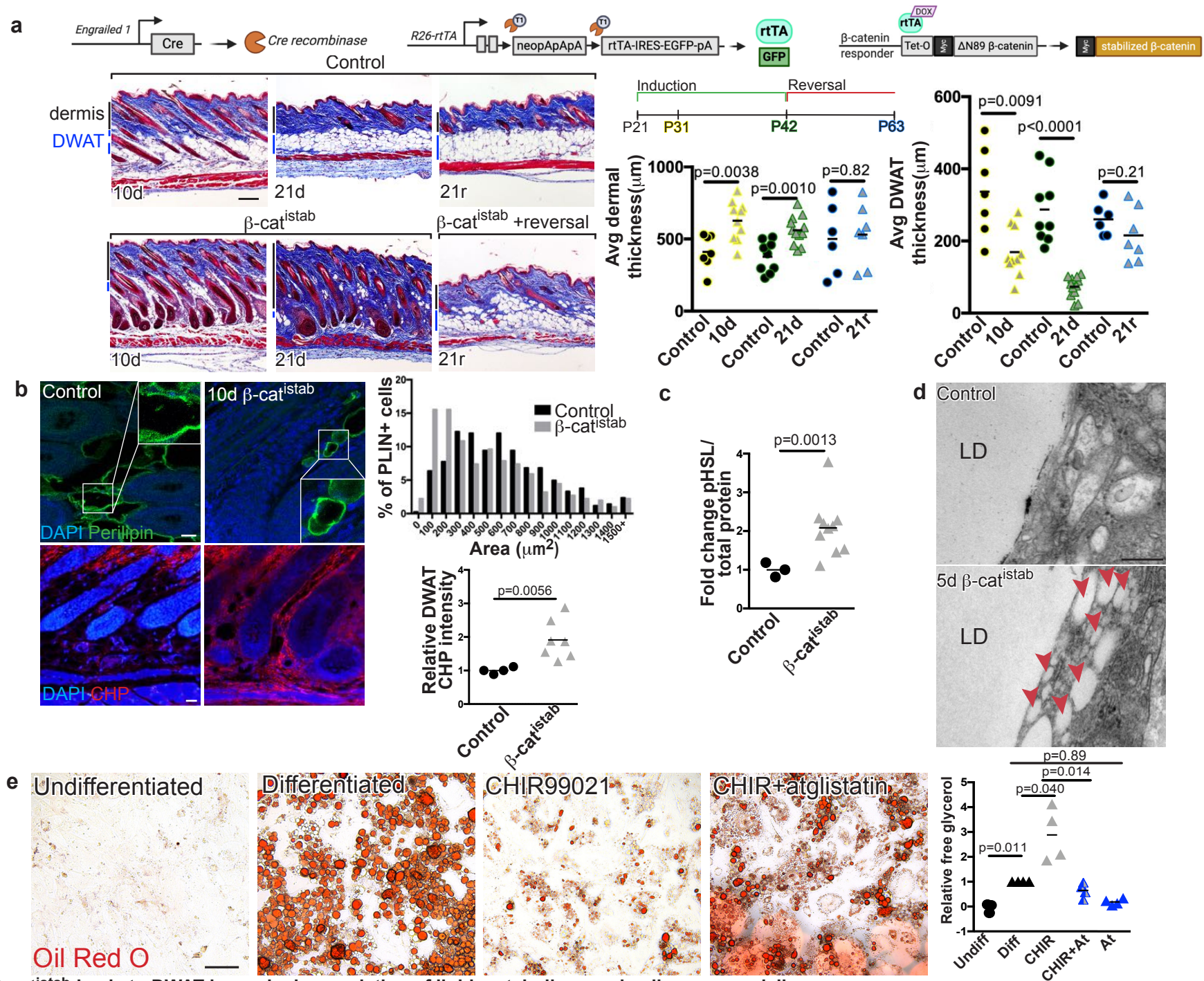**Fig. 3: β-cat[istab] leads to DWAT loss, via dysregulation of lipid metabolism, and collagen remodeling.**
a, Transgenes in doxycycline-inducible/reversible β-catenin (β-cat[istab]) dermal fibrosis model. Fibrosis progression in Masson's trichrome stained control (top) and β-cat[istab](bottom) dermis. Black and blue bars indicate dermal and DWAT thickness with quantification of average dorsal dermal and DWAT thickness/mouse. Scale bar=200μm (n=6-11). **b,** Indirect immunofluorescence of PLIN (green) and CHP stain (red) in control and 10d β-cat[istab] DWAT. Quantification of area of PLIN+ vesicles, 50/mouse (n=9). Relative corrected fluorescence CHP intensity in DWAT. Scale bar=25μm. **c,** Quantification of western blot for pHSL in control and 5d β-cat[istab] mouse skin relative to total protein (n=3-10). **d,** TEM images of control and 5d β-cat[istab] DWAT adipocytes. LD=large lipid droplet. Arrowheads=lipid vesicles. Scale bar=200nm. **e,** Primary mouse intradermal adipocyte progenitors untreated (Undifferentiated), treated with adipocyte induction media for 10d and subsequently with maintenance media (Differentiated) Wnt agonist (CHIR99021), or with CHIR99021 and ATGL inhibitor (atglistatin). Scale bar=200μm. Quantification of free glycerol between days 2 and 4 of treatment (n=4).
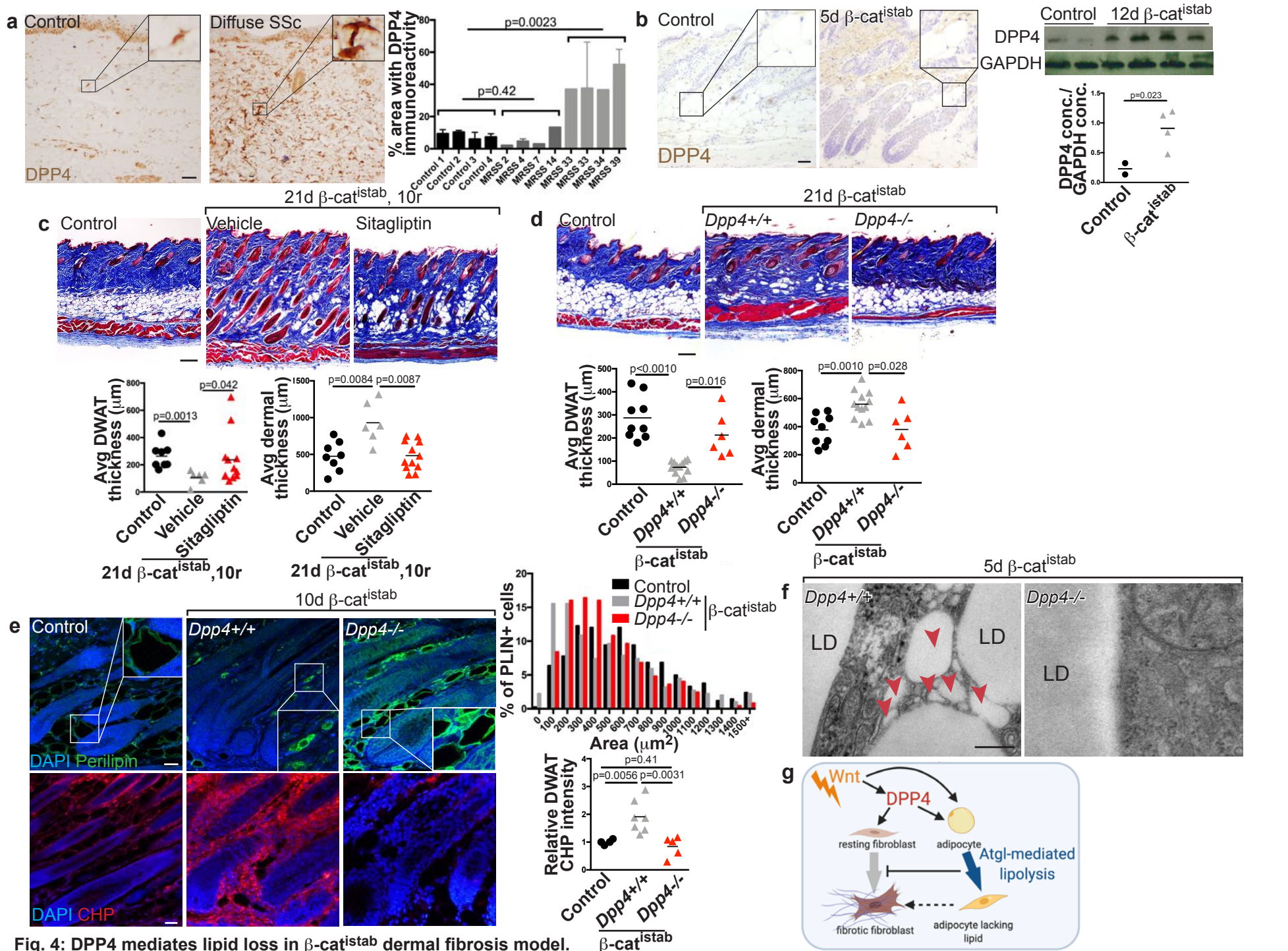
Fig. 4: DPP4 mediates lipid loss in β-cat^{istab} dermal fibrosis model.
a, DPP4 immunohistochemical staining of control and SSc human forearm skin. Scale bar=100μm. Accompanying quantification. **b,** DPP4 immunohistochemical staining on control and 5d β-cat^{istab} mouse skin. DPP4 protein expression relative to GAPDH protein quantity by western blot. Scale bar=100μm. **c,** Masson's trichrome stained mouse skin from control, 21d β-cat^{istab} and 10d reversal with vehicle or sitagliptin treatment. Scale bar= 200μm. Quantification of dermal and DWAT thickness/mouse (n= 5-12). **d,** Masson's trichrome stained dorsal skin of control, 21d β-cat^{istab}, and *Dpp4-/-* 21d β-cat^{istab}. Quantification of dermal and DWAT thickness/mouse (n= 6-10). Scale bar= 200μm. **e,** Indirect immunofluorescence staining for PLIN (green) and CHP staining (red) in mouse skin from control, 10d β-cat^{istab}, and *Dpp4-/-* 10d β-cat^{istab} mice with histogram of PLIN+ vesicle size (n=6-9) and DWAT CHP intensity measurement relative to control. Scale bar= 25μm. **f,** TEM images of DWAT adipocytes in *Dpp4+/+* 5d β-cat^{istab} and in *Dpp4-/-* 5d β-cat^{istab}. LD=large lipid droplet. Arrowheads= lipid vesicles. Scale bar =200nm. **g,** Working model.